Materials Advances

ROYAL SOCIETY OF CHEMISTRY

PAPER

View Article Online
View Journal | View Issue

Check for updates

Cite this: *Mater. Adv.*, 2022, 3, 3554

A new method of synthesis of Sb_2Se_3/rGO as a high-rate and low-temperature anode for sodium–ion batteries†

Lulu Hu,[a] Jun Pan,[b] Pei Zhao,[b] Gejun Shi,[a] Baofeng Wang *[a] and Fuqiang Huang *[bc]

Received 15th February 2022,
Accepted 2nd March 2022

DOI: 10.1039/d2ma00170e

rsc.li/materials-advances

Sodium–ion batteries (SIBs) are expected to replace lithium–ion batteries with low cost and high safety to become a new generation of energy storage equipment. Here, a novel precipitation transformation method is used to synthesize Sb_2Se_3 wrapped by reduced graphene oxide (rGO) as an anode for SIBs. These Sb_2Se_3 nanoparticles with a large surface area and multiple active sites can accelerate sodium ion diffusion and storage, resulting in high capacity and excellent rate performance. At the same time, rGO can alleviate the particle agglomeration of Sb_2Se_3 caused by volume expansion and increase the conductivity of the compound to improve charge transport. This synthesis method enables nanoscale and tight integration with rGO, synchronously satisfying the fast transport of ions and electrons, which provides conditions for the development of low-temperature performance. More importantly, Sb_2Se_3/rGO exhibits a capacity of 260 mA h g^{-1} at a current density of 20 A g^{-1} at room temperature. Even at −15 °C, the capacity retention remains at 38% at a current density of 2 A g^{-1}. Therefore, this precipitation transformation method can provide new ideas for synthesizing other compounds.

Introduction

Lithium-ion batteries as clean energy storage equipment have received extensive attention.[1–3] However, the lack of lithium resources limits the application of lithium-ion batteries in large-scale energy storage equipment. Sodium–ion batteries (SIBs) are promising energy cells because of the similarity of sodium ions to lithium ions and the advantages of rich and inexpensive sodium resources. The application of SIBs is still limited by low energy density/power density, poor low-temperature performance and so on.[4–7] Due to geographical location and climate, the temperature varies widely among regions. A battery may need to work in extreme environments, so exploring low-temperature battery materials is essential.[8,9] For the anode materials, the kinetics of sodium ions insertion is sluggish at low temperature (LT). There is a problem of asymmetry in charging and discharging, and the electrode material is heavily polarized at a high current density.[10,11] Therefore, it is urgent to improve the electrochemical performance at LT.

Compared with the low-capacity de-intercalation mechanism of carbon materials and the alloy-mechanism materials with large volume expansion, transformation mechanism materials can exhibit high capacity with relatively small volume expansion.[12,13] Common anode materials include oxides and sulfur (selenides). Sulfur (selenides) has higher reaction reversibilities and higher Coulombic efficiencies compared with oxides. Sb_2Se_3 can also work as an anode material with a theoretical specific capacity of 670 mA h g^{-1}, which is unmatched by carbon materials.[14–17] Moreover, both the conversion and alloy reactions are involved in the sodiation/desodiation process of Sb_2Se_3.[18,19] The product of the conversion reaction can be used as a buffer material for the alloy reaction to reduce the stress during particle pulverization. LT batteries require higher ionic and electronic conductivity of electrode materials. On the one hand, a composite with carbon material can improve the conductivity of the material and realize the rapid conduction of electrons.[20,21] On the other hand, nanoscale materials can shorten the ion transport path and achieve fast conduction of sodium ions.[15,22–24]

However, based on the crystal growth law of antimony selenide, it is easy to grow large rods and difficult to synthesize

[a] *Shanghai Key Laboratory of Materials Protection and Advanced Materials in Electric Power, Shanghai University of Electric Power, Shanghai 200090, China. E-mail: wangbaofeng@shiep.edu.cn*
[b] *State Key Laboratory of High Performance Ceramics and Superfine Microstructure, Shanghai Institute of Ceramics, Chinese Academy of Sciences, Shanghai 200050, China. E-mail: huangfq@mail.sic.ac.cn*
[c] *Beijing National Laboratory for Molecular Sciences and State Key Laboratory of Rare Earth Materials Chemistry and Applications, College of Chemistry and Molecular Engineering, Peking University, Beijing 100871, China*

† Electronic supplementary information (ESI) available. See DOI: 10.1039/d2ma00170e

nanoparticles.[24,25] Ou *et al.* synthesized a reduced graphene oxide (rGO)-overcoated Sb_2Se_3 nanorod anode for Na^+ battery, with a linear length of ≈600 nm and a diameter of ≈50 nm. After combining with rGO, the cycling performance of Sb_2Se_3/rGO is greatly improved, but due to the large Sb_2Se_3 nanorods, the rate performance is not satisfactory. At a current density of 2 A g^{-1}, the capacity retention was only 34% compared to that at 0.1 A g^{-1}.[15] Then, Fang *et al.* developed an ion-exchange method to synthesize Sb_2Se_3 microclips based on a microbelts template. Sb_2Se_3@PPy microclips exhibited improved cycling and rate performance. However, this anisotropic hollow structure is easily collapsed during cycling and agglomerates, thus hindering ionic conduction, and does not exhibit good electrochemical performance.[22] Therefore, it is important to use a new method to synthesize carbon–Sb_2Se_3 composite nanoparticles, to achieve fast conduction of ions and electrons simultaneously at LT.[26–30]

Here, a new precipitation transformation method is used to synthesize Sb_2Se_3 wrapped by rGO with controllable shape and size. The size of Sb_2Se_3 is only about 10 nm; such small nanoparticles with a large surface area can accelerate the reaction kinetics of sodium ion diffusion and storage, leading to high capacity and good rate performance. The addition of graphene can increase the conductivity and alleviate the particle agglomeration caused by volume expansion of Sb_2Se_3 in cycling. This structure design can realize fast conduction of electrons and ions, which is conducive to electrochemical performance.

Experimental section

Material synthesis

Sb_2Se_3/rGO was fabricated by a precipitation transformation method. Firstly, SnSe nanosheets were synthesized at room temperature. 79 mg Se and 20 g NaOH were dissolved in 50 ml deionized water. Secondly, 0.45 g $SnCl_2{\cdot}2H_2O$ and 10 g citric acid were dissolved in another 50 ml deionized water. The latter solution was added dropwise into the former under stirring until the solution turned black. SnSe nanosheets were collected by centrifugation, washing, and drying at 60 °C in a vacuum overnight. Next, graphene was obtained from graphite (Sinochem) using a modified Hummers' method,[31] and then 30 mg graphene and 0.1 g SnSe nanosheets were dissolved in 30 ml deionized water. 0.114 g $SbCl_3$ was dissolved in 10 ml alcohol and then added to the former solution under stirring. The solution was transferred into a Teflon-lined stainless autoclave and heated at 120 °C for 12 h. After centrifuging, washing, and drying, the powders were annealed at 400 °C for two hours in Ar/H_2 (95 : 5).

Structural characterization

X-Ray diffraction (XRD) patterns were acquired with an X-ray diffractometer (Bruker D8 Adv, Germany). X-ray photoelectron spectroscopy (XPS) data were obtained with an X-ray photoelectron spectrometer (ES CALAB250, USA). Transmission electron microscopy (TEM), high-resolution TEM (HRTEM), energy-dispersive X-ray spectrometry (EDS) as well as elemental mapping were conducted with transmission electron microscopes (JEOL GEM1011 or JEOL GEM-2100F, Japan). Scanning electron microscopy (SEM) images were obtained with a field-emission scanning electron microscope (Zeiss SUPRA55, Germany). Thermogravimetric analysis (TGA) was conducted with a Mettler Toledo TGA/SDTA851 thermal analyzer from 40 °C to 700 °C in air. N_2 sorption isotherms were performed with a Builder ASAP 2020 HD88 physisorption analyzer at 77 K.

Electrochemical measurements

The sodium-storage performances of the samples were tested with CR2032 coin cells. The working electrode was made of 70 wt% of the active materials, 20 wt% acetylene black, and 10 wt% of sodium alginate. The blend was milled for 30 min with droplets of deionized water to get a slurry. The slurry was spread on a clean copper foil and dried overnight in a vacuum at 60 °C. The loading mass of the active material was about 1 mg cm^{-2}. Coin cells were assembled using an Ar-filled glovebox (Mikrouna, Super 122017501900). 1.0 M $NaClO_4$ in ethylene carbonate and dimethyl carbonate (volume ratio of 1 : 1) containing 5% fluoroethylene carbonate was the electrolyte, Whatman GF/F glass microfibers were the separator, and Na foil was the counter and reference electrodes. Cyclic voltammetry (CV) curves were obtained using an electrochemical workstation (LK200A, China) at room-temperature. Galvanostatic discharge/charge profiles were measured on Land battery cyclers (Land CT2001A, China) between 0.01 and 2 V for SnSe nanosheets and 0.01 and 2.5 V for Sb_2Se_3/rGO at different temperatures. Electrochemical impedance spectra (EIS) were collected with an electrochemical workstation (Autolab PGSTAT 302N) in the frequency range of 100 kHz to 0.01 Hz.

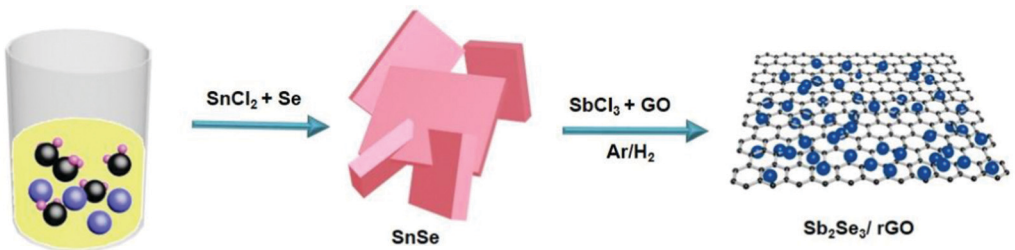

Scheme 1 The preparation process of Sb_2Se_3/rGO.

Results and discussion

Sb_2Se_3/rGO was synthesized *via* a precipitation transformation method, as illustrated in Scheme 1. First, pure SnSe nanosheets (Fig. S1 and S2, ESI†) were synthesized in a simple room-temperature method.[32] The SnSe nanosheets showed a size distribution with diameters of ~70 nm (Fig. S3, ESI†). Then Sb_2Se_3/rGO was made by adding $SbCl_3$ and graphene *via* a solvothermal reaction at 120 °C. The conversion mechanism is that the concentration of $SbCl_3$ is very large, and it reacts with Se^{2-} dissociated from SnSe. With the consumption of Se^{2-}, the reaction to form Sb_2Se_3 is promoted. As long as the content of Sn in the final component is not high, less than the Ksp of SnSe,[15] it exists in the form of ions and can be removed after washing steps. Finally, the composite was calcined at 400 °C in Ar/H_2, leading to the reduction of graphene to rGO.

The physical and chemical properties of the material are shown in Fig. 1. Fig. 1a shows the XRD pattern of Sb_2Se_3/rGO. It is noted that all the reflections come from the orthorhombic Sb_2Se_3 phase (JCPDS card no. 72-1184).[15] The peak at 26° originated from rGO, indicating the presence of rGO in the composite.[33,34] Further evidence comes from XPS spectra of Sb_2Se_3/rGO. Fig. 1b shows two peaks at 55.18 and 56.2 eV, which can be attributed to Se $3d_{3/2}$ and Se $3d_{5/2}$, respectively, indicating the presence of Se^{2-} in Sb_2Se_3.[35] As shown in Fig. 1c, the two peaks at 530.9 and 540.2 eV are assigned to Sb $3d_{3/2}$ and Sb $3d_{5/2}$ of Sb^{3+} in Sb_2Se_3. Another peak at 533.2 eV corresponds to O 1s, which can be attributed to the lesser oxidation of Sb_2Se_3 nanoparticles.[23] There are four peaks located at 284.6, 285.2, 286.6, and 289.2 eV from the high-resolution XPS spectrum of C 1s, owing to SP^{2-} bonded C–C, SP^{3-} bonded C–C, C═O and O═C–O, respectively (Fig. 1d).[28,36] The content of Sb_2Se_3 in the composite was examined by TGA. Fig. 1e shows the weight gain before 400 °C, assigned to the oxidation of Sb_2Se_3 to Sb_2O_4 and SeO_2. Next, weight loss is associated with the sublimation of SeO_2 and the oxidation of rGO (Fig. S4, ESI†). Through calculation, the content of Sb_2Se_3 in the composite is about 81 wt%. This result is in good agreement with the EDS spectrum (Fig. S5, ESI†). As shown in Fig. 1f, the specific surface area of Sb_2Se_3/rGO is measured by nitrogen adsorption–desorption isotherm, with a specific surface area of 58.3 m g^{-2} and an average pore size of ~25 nm, created by particle stacking. Although the large specific surface area reduces the initial Coulomb efficiency, it dramatically increases the migration speed of sodium ions.

The morphology characterization is shown in Fig. 2. Fig. 2a and b show SEM images of nanoparticles that are uniformly distributed on the surface of rGO. As shown in Fig. 2c and d, the size of Sb_2Se_3 nanoparticles is ~10 nm, and the tiny size could lead to large surface area, which is well matched with the better electrochemical performance. HRTEM image (Fig. 2e) shows clear lattice fringes with a spacing ~0.316 nm that could be attributed to (211) planes of Sb_2Se_3, which is in agreement with the XRD results in Fig. 1a. EDS element mapping can further reveal that both Sb and Se are uniformly distributed throughout the rGO, as illustrated in Fig. 2f. The size of Sb_2Se_3 is controllable through the adjustment of concentration, reaction time and temperature. The different size of Sb_2Se_3 particles means that the reaction kinetics is inconsistent, which in turn affects the electrochemical performance of the material. This will be described in the electrochemical performance section.

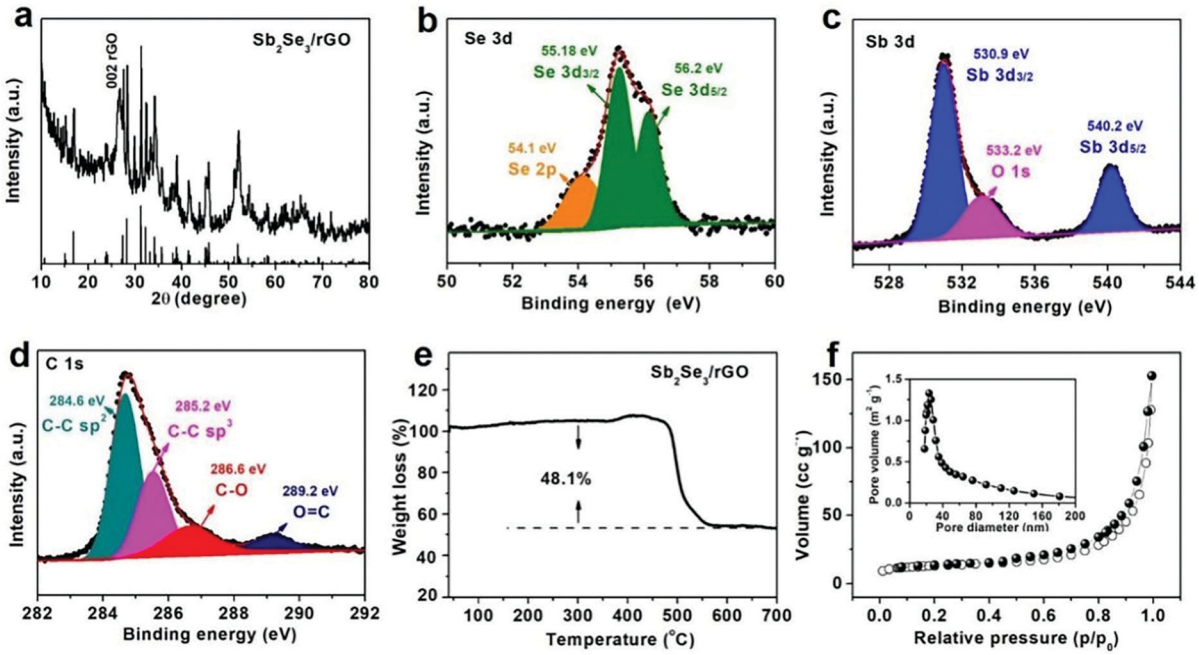

Fig. 1 Structural characterization. (a) XRD pattern. XPS spectra of (b) Se-3d; (c) Sb-3d; (d) C-1s of Sb_2Se_3/rGO. (e) TGA curve. (f) N_2 sorption isotherms and pore size distribution of Sb_2Se_3/rGO.

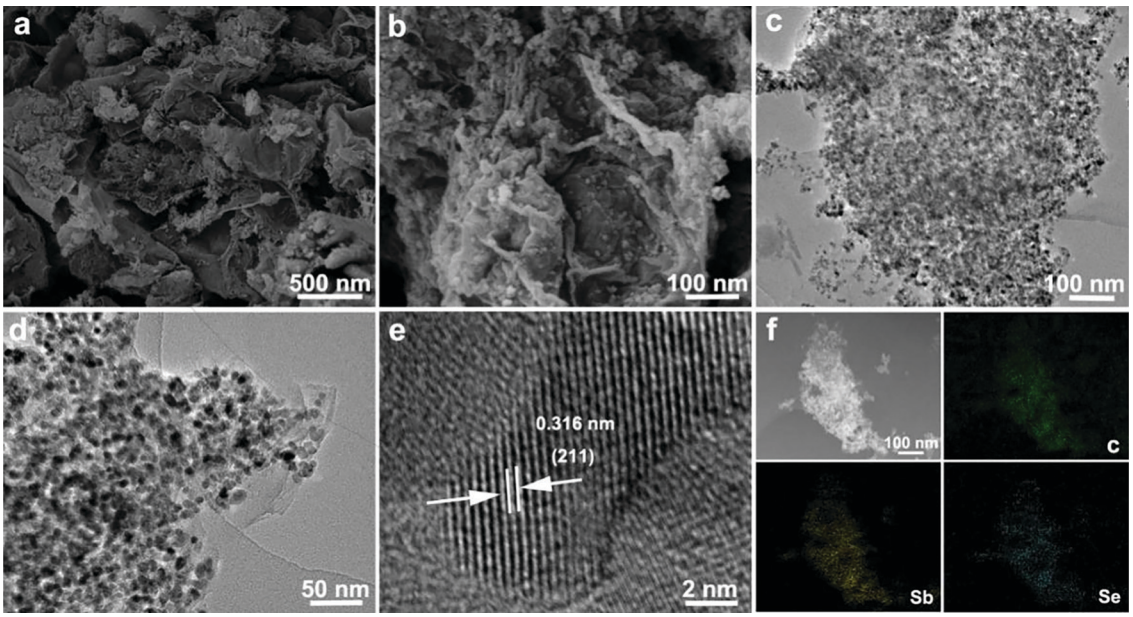

Fig. 2 Morphology characterization. (a and b) SEM images; (c and d) TEM images; (e) HRTEM image; (f) elemental mapping of Sb_2Se_3/rGO.

The reaction mechanism plays a decisive role in electrochemical performance. Hence, it is vital to explore the reaction mechanism. Sb_2Se_3/rGO is evaluated as an anode material in a half-cell of SIB. Fig. 3a shows CV curves of Sb_2Se_3/rGO during the first three cycles, where the broad cathodic peak centered at 0.98 V is attributed to the intercalation of Na ions into Sb_2Se_3 and the formation of Sb along with Na_2Se.[23] The peak over 0.2–0.7 V is correlated with the alloying reaction between Sb and Na, and the decomposition of electrolyte to form a solid-state interphase (SEI) film.[37–42] The anodic peaks located at 0.75 V and 1.25 V are attributed to the dealloying reaction of Na_3Sb to form Sb, followed by the conversion reaction between Sb and Na_2Se.[43,44] The broad peak around 1.8 V could correspond to the Na ions extracted from $Na_xSb_2Se_3$ to form Sb_2Se_3.[45,46] The following two cycles are matched well, indicating the excellent reversibility of Sb_2Se_3/rGO during alloying and conversion reactions. To clarify the reactions during sodiation/desodiation processes, *ex situ* HRTEM images of Sb_2Se_3/rGO were obtained. The *ex situ* HRTEM images were collected at different discharge/charge voltages in the first cycle.

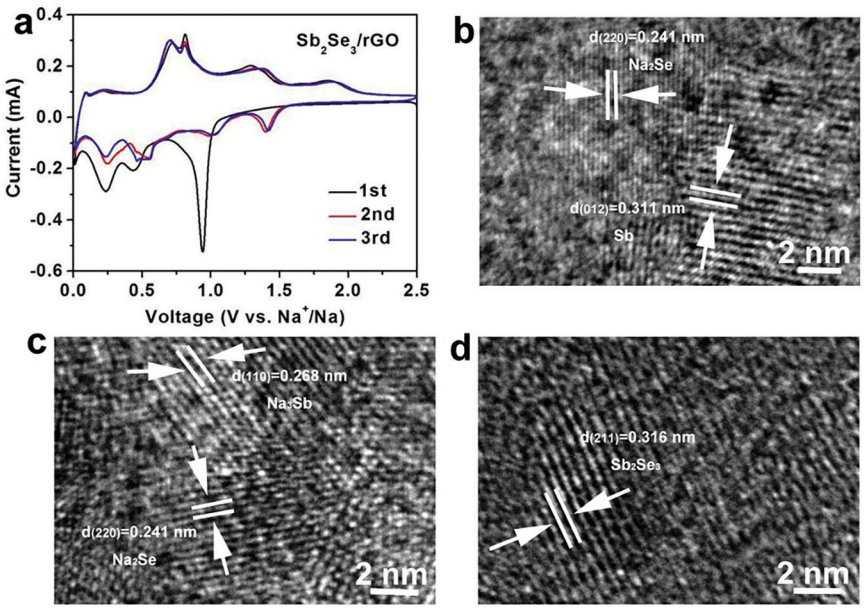

Fig. 3 Electrochemical mechanism analysis. (a) Cyclic voltammograms of Sb_2Se_3/rGO. HRTEM images of Sb_2Se_3/rGO: (b) discharged to 0.7 V; (c) fully discharged to 0.01 V; (d) fully charged to 2.5 V.

Fig. 3b shows an image of Sb_2Se_3/rGO discharged to 0.7 V. In this image, the lattice fringes of 0.311 nm and 0.241 nm can be attributed to (012) and (220) planes of Sb and Na_2Se, respectively. With the discharge voltage decreased to 0.01 V, the lattice fringes of Na_3Sb appeared (Fig. 3c), indicating the alloying reaction between Na ions and Sb. When fully charged to 2.5 V, the lattice fringes of the sample shown in Fig. 3d suggest that Sb_2Se_3 has formed, indicating the reversibility of the Sb_2Se_3/rGO anode for Na ion storage. All the results agree well with the CV curves in Fig. 3a.

The electrochemical properties of precursor (SnSe) and product (Sb_2Se_3/rGO) are shown in Fig. 4. SnSe nanosheets are a precursor material, and the cycle characteristics (Fig. S6, ESI†) and rate performances (Fig. S7, ESI†) were tested. SnSe nanosheets exhibit a capacity of 334 mA h g^{-1} at a current density of 0.5 A g^{-1} after 100 cycles. As a material with a nanosheet structure, the rate performance is good because of the fast reaction kinetics. The replacement of Sn by Sb is accompanied by the formation of nanoparticles, the capacity and kinetics being further improved. At the same time, rGO materials are introduced to increase conductivity and cycling stability. Through the structure design, high-rate and excellent low-temperature characteristics can be guaranteed. In order to obtain better electrochemical properties, many conditions have been tested, such as the amount of $SbCl_3$ added during the reaction (Fig. S8, ESI†), the temperature and time of the hydrothermal reaction (Fig. S9 and S10, ESI†), the calcination temperature in Ar/H_2 (Fig. S11, ESI†), and the cut-off voltage during charge/discharge (Fig. S12, ESI†). After optimization, Sb_2Se_3/rGO with the best electrochemical performance is selected. All of the following examinations are based on optimal conditions.

Fig. 4a shows the galvanostatic charge/discharge curves for the first three cycles. The cathodic/anodic peaks in CV curves match well with the charge/discharge plateaus. As we can see from the first-cycle charge/discharge curve, the initial Coulombic efficiency is ~67.3%. The capacity loss comes from the decomposition of electrolytes, the formation of SEI film, and so on.[47,48] In the following cycles, the capacity is almost unchanged, indicating the good reversibility of the compound. Fig. 4b shows the cycling performance of Sb_2Se_3/rGO within 0.01–2.5 V at a current density of 0.5 A g^{-1}. It indicates that the composite exhibits a reversible capacity at 511 mAh g^{-1} after 50 cycles. As shown in Fig. S13 (ESI†), the capacity of rGO is about 75 mA h g^{-1} at a current density of 0.5 A g^{-1}. The theoretical specific capacity of Sb_2Se_3/rGO composite is 75 mA h g^{-1}*19% + 670 mAh g^{-1} × 81% = 557 mA h g^{-1}, which is consistent with the results in Fig. 4b. The excellent rate performance is shown in Fig. 4c. The capacity of Sb_2Se_3/rGO is 580.6 mA h g^{-1} at 0.1 A g^{-1}, 547 mA h g^{-1} at 0.2 A g^{-1}, 517.5 mA h g^{-1} at 0.5 A g^{-1}, 498.8 mA h g^{-1} at 1 A g^{-1}, 467.9 mA h g^{-1} at 2 A g^{-1}, 396.8 mA h g^{-1} at 5 A g^{-1}, and 311 mA h g^{-1} at 10 A g^{-1}. Even at a high current density of 20 A g^{-1}, it still has a capacity of 266.5 mA h g^{-1} with a capacity retention of 46% related to the discharge capacity at 0.1 A g^{-1}. This is in good agreement with the large surface area and multiple active sites of small Sb_2Se_3 nanoparticles, which accelerate Na ion diffusion kinetics.[49] It is found that the rate performance of Sb_2Se_3/rGO is superior to that of previously reported Sb_2Se_3 in SIBs (Fig. 4d), including polypyrrole-coated Sb_2Se_3 microclips (486 mA h g^{-1} at 2 A g^{-1}),[20] Sb_2Se_3 nanowires (247 mA h g^{-1} at 2 A g^{-1}),[23] capsular carbon shell-encapsulated Sb_2Se_3 (398.7 mA h g^{-1} at 2 A g^{-1}),[24] and carbon nanofibers

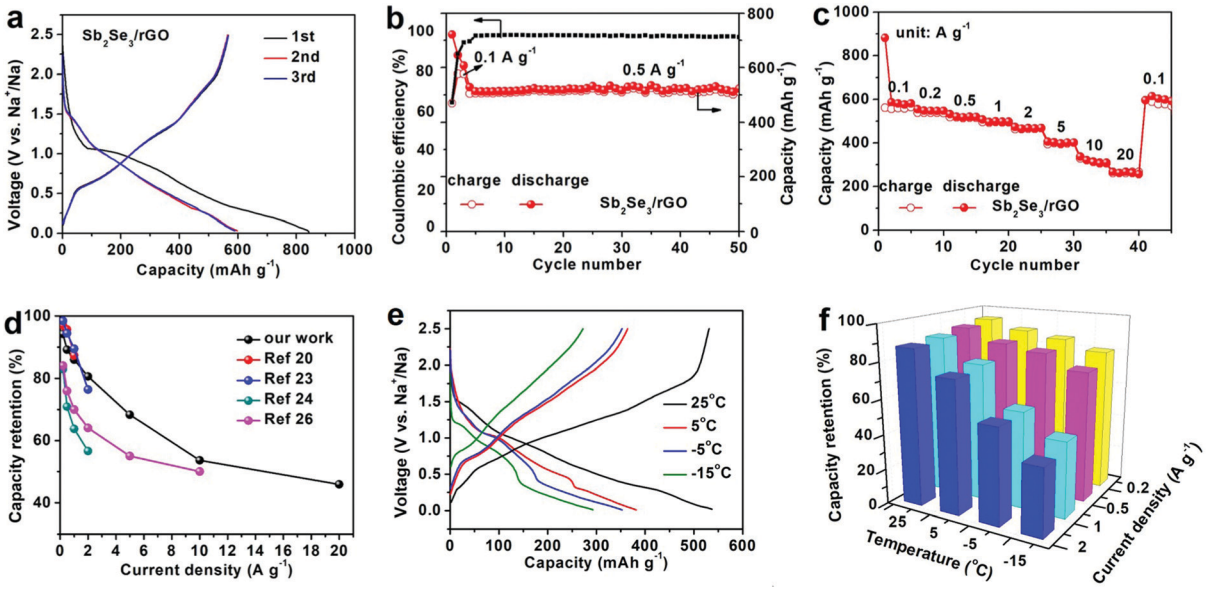

Fig. 4 Electrochemical performances. (a) Discharge/charge curves of Sb_2Se_3/rGO at a current density of 0.1 A g^{-1}. (b) Cycling performance and (c) rate performance of Sb_2Se_3/rGO. (d) Comparison of results of reported works with ours in terms of capacity retention. (e) Discharge/charge curves of Sb_2Se_3/rGO at different temperatures. (f) The capacity retentions of Sb_2Se_3/rGO along with temperature variations between 25 and −15 °C at a various current densities of 0.2, 0.5, 1, and 2 A g^{-1}.

with embedded Sb_2Se_3 nanoparticles (250 mA h g^{-1} at 10 A g^{-1}).[26] To understand the excellent electrochemical performances of Sb_2Se_3/rGO in SIBs, EIS was measured at open circuit potential (OCP) and 2.5 V after five cycles (Fig. S13, ESI†). It is fitted by an equivalent circuit (Table S1, ESI†). Sb_2Se_3/rGO presents a smaller charge-transfer resistance (R_{ct}) after five cycles. The result is associated with the faster interface kinetics, resulting in excellent rate performance.[50] However, R_{ct} after 100 cycles is greater than after 5 cycles, because of the continuous thickening of the SEI film and the agglomeration caused by the structural destruction of Sb_2Se_3, causing a slowed ion conduction. In addition to the excellent rate performance, the composite also displays outstanding LT performance. Fig. 4e shows the discharge curves tested under various temperatures from 25 °C to −15 °C at a current density of 0.1 A g^{-1}. With a drop in temperature, the capacity gradually decreases. This can be associated with the difficult sodiation and serious polarization of the electrode at LT.[51] The discharge curves also show an increase in polarization voltage. The main reason is the slow desolvation of Na^+ ions and the slow transport of Na^+ ions in the electrode material. The LT performance of SnSe was also tested (Fig. S14, ESI†). Fig. 4f shows the capacity retentions at different discharge current densities (0.1, 0.2, 0.5, 1, and 2 A g^{-1}) and testing temperatures (from 25 °C to −15 °C). The capacity retention at −15 °C compared to that at 25 °C is ∼77.5% at 0.2 A g^{-1} and ∼43% at 2 A g^{-1}. This result is better than that of SnSe tested at the same condition (Fig. S15, ESI†), proving the importance of our structural design.

Conclusions

In summary, Sb_2Se_3/rGO is synthesized by the precipitation transformation method with controllable shape and size. This composite exhibits an outstanding rate performance owing to small Sb_2Se_3 nanoparticles with an increase of specific surface area and increase of active sites. The diffusion and storage of sodium ions become more rapid, resulting in good rate performance. What is more, rGO can alleviate the particle agglomeration caused by volume expansion of Sb_2Se_3 and increase the conductivity of the compound. This synthesis strategy can tightly bind Sb_2Se_3 nanoparticles to rGO, and achieve fast conduction of ions and electrons simultaneously. As for the rate capability, the composite exhibits a reversible capacity of 266 mAh g^{-1} at 20 A g^{-1}. Even at −15 °C, the capacity retention remains at 38% at a current density of 2 A g^{-1}. All those data indicate that this composite structure has promising potential in low-temperature SIBs. In the future, the precipitation transformation conversion method could be widely used in the synthesis of other composite nanomaterials.

Author contributions

Lulu Hu: methodology, formal analysis, investigation, writing – original draft, resources. Jun Pan: conceptualization, investigation, data curation, writing – original draft, writing – review & editing, supervision. Pei Zhao: draft curation, supervision. Gejun Shi: data curation, supervision. Baofeng Wang: investigation, funding acquisition, resources, writing – review & editing. Fuqiang Huang: methodology, writing – review & editing, supervision, project administration, funding acquisition.

Conflicts of interest

The authors declare that they have no known competing financial interests or personal relationships that could have appeared to influence the work reported in this paper.

Acknowledgements

This work is financially supported by the National Natural Science Foundation of China (No. 22075173), the Science and Technology Commission of Shanghai Municipality (No. 19DZ2271100 and 21010501100), the Key Research Program of Frontier Science of the Chinese Academy of Sciences (Grant No. QYZDJ-SSW-JSC013), and the Super Post-Doctoral Fellow Program of Shanghai (E01SCB17).

References

1 J. Xie and Y. C. Lu, A retrospective on lithium-ion batteries, *Nat. Commun.*, 2020, **11**, 2499.
2 Y. J. Fan, D. Y. Luan, S. Y. Gao and X. W. Lou, Rational design and engineering of one-dimensional hollow nanostructures for efficient electrochemical energy storage, *Angew. Chem., Int. Ed.*, 2021, **60**, 20102–20118.
3 F. X. Wu, J. Maier and Y. Yu, Guidelines and trends for next-generation rechargeable lithium and lithium-ion batteries, *Chem. Soc. Rev.*, 2020, **49**, 1569–1614.
4 P. K. Nayak, L. Yang, W. Brehm and P. Adelhelm, From Lithium-Ion to Sodium-Ion Batteries: Advantages, Challenges, and Surprises, *Angew. Chem., Int. Ed.*, 2018, **57**, 102–120.
5 J. Y. Hwang, S. T. Myung and Y. K. Sun, Sodium-ion batteries: present and future, *Chem. Soc. Rev.*, 2017, **46**, 3529–3614.
6 D. R. Deng, X. Y. Cui, Q. H. Wu, M. S. Zheng and Q. F. Dong, *In situ* synthesis TiO_2 nanosheets@rGO for ultrafast sodium ion storage at both room and low temperatures, *J. Alloys Compd.*, 2020, **835**, 155413.
7 A. L. Zhao, Y. J. Fan, X. P. Ai, H. X. Yang and Y. L. Cao, Mixed polyanion cathode materials: Toward stable and high-energy sodium-ion batteries, *J. Energy Chem.*, 2021, **60**, 635–648.
8 Y. Y. Wang, B. H. Hou, J. Z. Guo, Q. L. Ning, W. L. Pang, J. Wang, C. L. Lü and X. L. Wu, An ultralong lifespan and low-temperature workable sodium-ion full battery for stationary energy storage, *Adv. Energy Mater.*, 2018, **8**, 1703252.
9 H. L. Zhu, F. Shen, W. Luo, S. Z. Zhu, M. H. Zhao, B. Natarajan, J. Q. Dai, L. H. Zhou, X. L. Ji, R. S. Yassar, T. Li and L. B. Hu, Low temperature carbonization of cellulose nanocrystals for high performance carbon anode of sodium-ion batteries, *Nano Energy*, 2017, **33**, 37–44.

10 J. Z. Guo, P. F. Wang, X. L. Wu, X. H. Zhang, Q. Yan, H. Chen, J. P. Zhang and Y. G. Guo, High-energy/power and low-temperature cathode for sodium-Ion batteries: in situ XRD study and superior full-cell performance, *Adv. Mater.*, 2017, **29**, 1701968.

11 B. H. Hou, Y. Y. Wang, D. S. Liu, Z. Y. Gu, X. Feng, H. Fan, T. Zhang, C. Lü and X. L. Wu, N-doped carbon-coated Ni1.8Co1.2Se4 nanoaggregates encapsulated in N-doped carbon nanoboxes as advanced anode with outstanding high-rate and low-temperature performance for sodium-ion half/full batteries, *Adv. Funct. Mater.*, 2018, **28**, 1805444.

12 L. C. Wang, J. Swiatowska, S. R. Dai, M. L. Cao, Z. C. Zhong, Y. Shen and M. K. Wang, Promises and challenges of alloy-type and conversion-type anode materials for sodium-ion batteries, *Mater. Today Energy*, 2019, **11**, 46–60.

13 Y. J. Fang, D. Y. Luan and X. W. Lou, Recent advances on mixed metal sulfides for advanced sodium-ion batteries, *Adv. Mater.*, 2020, **32**, 2002976.

14 Z. Yang, J. Y. Sun, Y. Z. Ni, Z. H. Zhao, J. M. Bao and S. Chen, Facile synthesis and *in situ* transmission electron microscopy investigation of a highly stable Sb_2Te_3/C nanocomposite for sodium–ion batteries, *Energy Storage Mater.*, 2017, **9**, 214–220.

15 X. Ou, C. H. Yang, X. H. Xiong, F. H. Zheng, Q. C. Pan, C. Jin, M. L. Liu and K. Huang, A new rGO-overcoated Sb_2Se_3 nanorods anode for Na^+ battery: in situ X-Ray diffraction study on a live sodiation/desodiation process, *Adv. Funct. Mater.*, 2017, **27**, 1606242.

16 J. Ding, H. L. Wang, Z. Li, A. Kohandehghan, K. Cui, Z. W. Xu, B. Zahiri, X. H. Tan, E. M. Lotfabad, B. C. Olsen and D. Mitlin, Carbon nanosheet frameworks derived from peat moss as high performance sodium ion battery anodes, *ACS Nano*, 2013, **7**, 11004–11015.

17 G. H. Chen, J. Zhou, J. Zuo and Q. Yang, Organometallically anisotropic growth of ultralong Sb_2Se_3 nanowires with highly enhanced photothermal response, *ACS Appl. Mater. Interfaces*, 2016, **8**, 2819–2825.

18 Y. Wu, W. Luo, P. Gao, C. Y. Zhu, X. B. Hu, K. Qu, J. Chen, Y. Q. Wang, L. T. Sun, L. Q. Mai and F. Xu, Unveiling the microscopic origin of asymmetric phase transformations in (de)sodiated Sb_2Se_3 with in situ transmission electron microscopy, *Nano Energy*, 2020, **77**, 105299.

19 L. Guo, L. Y. Cao, J. F. Huang, J. Y. Li and S. Y. Chen, Carbon capsule confined Sb_2Se_3 for fast Na^+ extraction in sodium-ion batteries, Sustain, *Energy Fuels*, 2020, **4**, 797–808.

20 Z. J. Cao, X. B. Ma, W. H. Dong and H. L. Wang, FeS@tubular mesoporous carbon as high capacity and long cycle life anode materials for lithium- and sodium-ions batteries, *J. Alloys Compd.*, 2019, **786**, 523–529.

21 P. Ge, X. Y. Cao, H. S. Hou, S. J. Li and X. B. Ji, Rodlike Sb_2Se_3 wrapped with carbon: the eploring of electrochemical properties in sodium-ion batteries, *ACS Appl. Mater. Interfaces*, 2017, **9**, 34979–34989.

22 Y. J. Fang, X. Y. Yu and X. W. Lou, Formation of polypyrrole-coated Sb_2Se_3 microclips with enhanced sodium-storage properties, *Angew. Chem., Int. Ed.*, 2018, **57**, 9859–9863.

23 Q. Q. Li, P. S. Du, Y. F. Yuan, W. T. Yao, Z. T. Ma, B. K. Guo, Y. C. Lyu, P. Wang, H. T. Wang, A. M. Nie, R. Shahbazian-Yassar and J. Lu, Real-time TEM study of nanopore evolution in battery materials and their suppression for enhanced cycling performance, *Nano Lett.*, 2019, **19**, 3074–3082.

24 L. Guo, L. Y. Cao, J. F. Huang, Y. Wang, W. B. Li, H. Qi, S. Y. Chen and J. Y. Li, Design of an ultra-stable Sb_2Se_3 anode with excellent Na storage performance, *J. Alloys Compd.*, 2019, **810**, 151930.

25 Y. J. Fang, X. Y. Yu and X. W. Lou, Formation of polypyrrole-coated Sb_2Se_3 microclips with enhanced sodium-storage properties, *Angew. Chem., Int. Ed.*, 2018, **57**, 9859–9863.

26 L. S. Xia, Z. D. Yang, B. Tang, F. Li, J. P. Wei and Z. Zhou, Carbon nanofibers with embedded Sb_2Se_3 nanoparticles as highly reversible anodes for Na-ion batteries., *Small*, 2021, **17**, 2006016.

27 F. E. Niu, J. Yang, N. N. Wang, D. P. Zhang, W. L. Fan, J. Yang and Y. T. Qian, MoSe2-covered N,P-doped carbon nanosheets as a long-life and high-rate anode material for sodium-ion batteries, *Adv. Funct. Mater.*, 2017, **27**, 1700522.

28 R. F. Nie, J. J. Shi, W. C. Du, W. S. Ning, Z. Y. Hou and F. S. Xiao, A sandwich N-doped graphene/Co_3O_4 hybrid: an efficient catalyst for selective oxidation of olefins and alcohols, *J. Mater. Chem. A*, 2013, **1**, 9037–9045.

29 W. J. Zhao, M. J. Li, Y. B. Qi, Y. J. Tao, Z. P. Shi, Y. J. Liu and J. P. Cheng, Ultrasound sonochemical synthesis of amorphous Sb_2S_3-graphene composites for sodium-ion batteries, *J. Colloid Interface Sci.*, 2021, **586**, 404–411.

30 H. Q. Wang, L. Gou, W. F. Jing, D. An, Y. Li, M. Wang, N. Li, S. L. Hu and Y. B. He, Highly microporous $SbPO_4$/BC_x hybrid anodes for sodium-ion batteries, *Mater. Adv.*, 2020, **1**, 206–214.

31 Y. Wen, K. He, Y. J. Zhu, F. D. Han, Y. H. Xu, I. Matsuda, Y. Ishii, J. Cumings and C. S. Wang, Expanded graphite as superior anode for sodium-ion batteries, *Nat. Commun.*, 2014, **5**, 4033.

32 S. Yuan, Y. H. Zhu, W. Li, S. Wang, D. Xu, L. Li, Y. Zhang and X. B. Zhang, Surfactant-free aqueous synthesis of pure single-crystalline SnSe nanosheet clusters as anode for high energy-and power-density sodium-ion batteries, *Adv. Mater.*, 2017, **29**, 1602469.

33 H. T. Yuan, X. G. Liu, F. Afshinmanesh, W. Li, G. Xu, J. Sun, B. Lian, A. G. Curto, G. J. Ye, Y. Hikita, Z. X. Shen, S. C. Zhang, X. H. Chen, M. Brongersma, H. Y. Hwang and Y. Cui, Polarization-sensitive broadband photodetector using a black phosphorus vertical p–n junction, *Nat. Nanotechnol.*, 2015, **10**, 707–713.

34 M. Patel, H. Haroon, A. Kumar, J. Ahmad, G. A. Bhat, S. Lone, D. Putthusseri, K. Majid and M. Wahid, High Na^+ mobility in rGO wrapped high aspect ratio 1D SbSe nano structure renders better electrochemical Na^+ battery performance, *ChemPhysChem*, 2020, **21**, 814–820.

35 S. L. Xin, Z. Q. Liu, L. Ma, Y. Sun, C. H. Xiao, F. Li and Y. P. Du, Visualization of the electrocatalytic activity of three-dimensional $MoSe_2$@reduced graphene oxide hybrid

nanostructures for oxygen reduction reaction, *Nano Res.*, 2016, **9**, 3795–3811.

36 M. Wang, Z. Z. Yang, W. H. Li, L. Gu and Y. Yu, Superior sodium storage in 3D interconnected nitrogen and oxygen dual-doped carbon network, *Small*, 2016, **12**, 2559–2566.

37 J. Pan, N. N. Wang, Y. L. Zhou, X. F. Yang, W. Y. Zhou, Y. T. Qian and J. Yang, Simple synthesis of a porous Sb/Sb_2O_3 nanocomposite for a high-capacity anode material in Na-ion batteries, *Nano Res.*, 2017, **10**, 1794–1803.

38 R. Kumar, P. Lu, X. Xiao, Z. Huang and B. W. Sheldon, Strain-induced lithium losses in the solid electrolyte interphase on silicon electrodes, *ACS Appl. Mater. Interfaces*, 2017, **9**, 28406–28417.

39 S. Bhattacharya, A. R. Riahi and A. T. Alpas, Electrochemical cycling behaviour of lithium carbonate (Li_2CO_3) pre-treated graphite anodes-SEI formation and graphite damage mechanisms, *Carbon*, 2014, **77**, 99–112.

40 L. S. Xia, Z. D. Yang, B. Tang, F. Li, J. P. Wei and Z. Zhou, Carbon nanofibers with embedded Sb_2Se_3 nanoparticles as highly reversible anodes for Na-ion batteries, *Small*, 2021, **17**, 2006016.

41 S. Sarkar and S. C. Peter, An overview on Sb-based intermetallics and alloys for sodium-ion batteries: trends, challenges and future prospects from material synthesis to battery performance, *J. Mater. Chem. A*, 2021, **9**, 5164–5196.

42 X. L. Qiu, X. L. Wang, Y. X. He, J. Y. Liang, K. Liang, B. L. Tardy, J. J. Richardon, M. Hu, H. Wu, Y. Zhang, O. J. Rojas, I. Manners and J. L. Guo, Superstructured mesocrystals through multiple inherent molecular interactions for highly reversible sodium ion batteries, *Sci. Adv.*, 2021, **7**, eabh3482.

43 D. K. Yu and C. M. Park, Sb-based intermetallics and nanocomposites as stable and fast Na-ion battery anodes, *Chem. Eng. J.*, 2021, **409**, 127380.

44 J. Pan, S. L. Chen, Q. Fu, Y. W. Sun, Y. C. Zhang, N. Lin, P. Gao, J. Yang and Y. Y. Qian, Layered-structure $SbPO_4$/reduced graphene oxide: a new advanced anode material for sodium ion batteries, *ACS Nano*, 2018, **12**, 12869–12878.

45 Y. Y. Lu, N. Zhang, S. Jiang, Y. D. Zhang, M. Zhou, Z. L. Tao, L. A. Archer and J. Chen, High-capacity and ultrafast Na-ion storage of a self-supported 3D porous antimony persulfide-graphene foam architecture, *Nano Lett.*, 2017, **17**, 3668–3674.

46 J. Lin, L. X. Yao, C. Y. Zhang, H. R. Ding, Y. H. Wu, S. Li, J. J. Han, G. H. Yue and D. L. Peng, Construction of Sb_2S_3@SnS@C tubular heterostructures as high-performance anode materials for sodium-ion batteries, *ACS Sustainable Chem. Eng.*, 2021, **9**, 11280–11289.

47 M. J. Hu, Y. Z. Jiang, W. P. Sun, H. T. Wang, C. H. Jin and M. Yan, Reversible conversion-alloying of Sb_2O_3 as a high-capacity, high-rate, and durable anode for sodium ion batteries, *ACS Appl. Mater. Interfaces*, 2014, **6**, 19449–19455.

48 Y. H. Du, Y. F. Zhang, L. Li, N. Wang and Y. J. Chai, Nano SnO2 and Sb_2O_3 combined with CNTs as a high-capacity lithium storage material, *Appl. Surf. Sci.*, 2021, **543**, 148870.

49 L. Guo, L. Y. Cao, J. F. Huang, J. Y. Li, K. Kajiyoshi, J. J. He and H. Qi, Guiding fabrication of continuous carbon-confined Sb_2Se_3 nanoparticle structure for durable potassium-storage performance, *ACS Appl. Energy Mater.*, 2021, **4**, 10391–10403.

50 P. Zhang, F. R. Qin, L. Zou, M. R. Wang, K. Zhang, Y. Q. Lai and J. Li, Few-layered MoS_2/C with expanding d-spacing as a high-performance anode for sodium-ion batteries, *Nanoscale*, 2017, **9**, 12189–12195.

51 G. B. Liu, S. M. Li, J. Mei, L. M. Liu, Y. H. Cui and H. Liu, New insights into low temperature properties of Li-rich layered cathode materials, *J. Power Sources*, 2017, **353**, 51–57.